October 1992

EQUILIBRIUM AND SPACE-CHARGE WAVE ANALYSIS OF ELECTRON BEAMS IN CONDUCTING AND ABSORBING GYROTRON BEAM TUNNELS

D.R. Whaley and M.Q. Tran

Equilibrium and Space-Charge Wave Analysis of Electron Beams in Conducting and Absorbing Gyrotron Beam Tunnels

D. R. Whaley,   M. Q. Tran

Centre de Recherches en Physique des Plasmas,
Association Euratom-Confédération Suisse,
Ecole Polytechnique Fédérale de Lausanne, 21 Av. des Bains,
CH-1007 Lausanne, Switzerland

The fluid equations for an electron beam are used to calculate the equilibrium velocity and density profiles, limiting current and space-charge wave properties of an annular beam undergoing magnetic compression in a gyrotron beam tunnel. Both non-relativistic and relativistic equations are derived. The beam tunnel may have a conventional smooth wall or an absorbing dielectric-loaded wall. Small values of magnetic compression are seen to have a large effect on the profiles and the current limit of a given tunnel. Common dielectric-loaded tunnels are also seen to reduce the limiting current by *5% - 20%*. Limiting current data for a wide range of beam parameters are shown. The dispersion relation for a convective instability arising from the gradient in the equilibrium potential depression profiles is derived using the linearized fluid equations. The growth rate is seen to increase for increasing current and pitch angle, and for increasing wall effects of an absorbing tunnel. The average growth rate is calculated for a typical gyrotron beam and beam tunnel as well as for a beam entering an interaction cavity. Growth rates for all values of k_z are seen to decrease to zero for a conventional conducting beam tunnel in a constant magnetic field.

I. Introduction

Characteristics of electron flow from cathode to collector is of interest in the design of present-day gyrotrons. Beam tunnels are commonly included in the design and provide a conducting, grounded wall near the beam as it propagates from the cathode to the interaction cavity. This tunnel is designed to keep the potential depression of the beam at a minimum since the space charge of a beam creates a self-potential through which the beam must pass. This self-potential affects the equilibrium velocity and density profiles and if rises too high, a barrier forms and transmission becomes impossible. These profiles and ultimately the limiting current depend on details of the beam, of the beam tunnel, and of the magnetic field compression along the beam path. The maximum beam current which can pass through a beam tunnel at constant magnetic field as a function of beam energy and pitch angle has been calculated by several authors (Drobot *et al.* 1981, Ganguly *et al.* 1984, for example). These calculations have been performed at constant tunnel magnetic field and axial variations are not considered. Often, though, a beam experiences magnetic compression and changing wall conditions as it passes through the tunnel before it reaches the constant-B cavity interaction region. In this paper the effect of this axial variation is included in the calculation of velocity and density profiles and of limiting current.

Often the beam tunnel is highly overmoded for the design frequency of the gyrotron (i.e. $f_{co} < f_0$). Reflected gyrotron power is therefore able to propagate in the beam tunnel and may undergo a resonant interaction with the beam before it reaches the cavity. Parasitic excitation may also develop and create enough power to affect beam properties. These beam-wave interactions are thought, under certain conditions, to alter the beam characteristics from those necessary for efficient cavity coupling. It is therefore common to use a beam tunnel consisting of an absorbing material which attenuates this unwanted microwave power before it can interact with the beam (Lawson *et al.* 1990, Alberti

1991). The absorbing structure however may affect the electron flow. This paper therefore also examines how an absorbing beam tunnel alters the equilibrium velocity and density profiles, limiting current and stability of gyrotron electron beams. Section II defines the geometry of the absorbing tunnel and shows a specific case for an actual beam tunnel used at the CRPP. Section III presents a method for calculating the self-consistent axial velocity and density profiles and potential-depression limited current using the fluid model equations allowing for both a conventional (smooth conducting) and an absorbing beam tunnel. This is performed for both non-relativistic and relativistic models and includes effects of magnetic-field compression along the beam path. In Sec. IV a macroscopic fluid instability is discussed which is brought about by the density gradient viewed by the beam as it traverses the beam tunnel. This gradient is due to the geometry and material of the absorbing wall and to the magnetic field profile. The dispersion relation shows that the growth rate for this instability is dependent on the magnitude of the potential oscillations and on the beam current, size, and pitch angle. Concluding remarks are presented in Sec. V.

II. Geometry

An absorbing beam tunnel is commonly made of alternating rings of conducting copper and absorbing dielectric. These tunnels, or variations of them, are used in nearly all gyrotrons. The geometry of such a tunnel is shown in Figs. 1(a) and (b). The conducting rings serve to conduct away any charge which might be intercepted by the tunnel walls and the dielectric is recessed so as not to build up surface charge. Microwave absorption in these structures can be computed at a given frequency for any given TE or TM mode (Latham 1990). The relative dielectric constant of the absorbing material is usually quite high (>5) and therefore the potential on the surface of the dielectric facing the beam remains low. The effective radius of the tunnel as seen by the beam then oscillates as the beam moves axially. The result of this oscillation is an axially

oscillating beam potential depression, true even for constant axial beam density. In Figs. 2, Poisson's equation, $\nabla^2 \phi = -\rho/\varepsilon_0$, is used to compute potential profiles for a section of a tunnel used at the CRPP, the geometry and potential contours of which are shown in Fig. 2(a). The beam characteristics and tunnel dimensions are given in the figure. Here a beam density constant in r is assumed whose value varies axially conserving current and magnetic moment. A Neumann boundary condition ($\nabla_z \phi = 0$) is used at the tunnel ends. The value of the potential along the beam path for constant density at $r = r_b - \Delta r/2$ is plotted in Fig. 2(c) (solid curve). Even for a flat axial density profile (Fig. 2(b) solid curve) the computed potential profile is seen to oscillate. The oscillations in the potential profile cause β_z to be locally lower between the conducting rings where the potential is high. This then leads to charge bunching between the rings which further lowers β_z. This charge bunching and subsequent axial peaking of the potential depression will create a current limit lower than that of a smooth wall tunnel. If the constant density solution is iterated to account for this potential depression, $\beta_z^2 = \beta_{z_0}^2 - 2q\phi/mc^2$, the self-consistent solution is found as shown in Fig. 2(b-c) (dotted curves). Here, $\beta_z = v_z/c$ where v_z is the axial velocity and c is the speed of light. All subscripted zeros of Secs. II and III indicate conditions at the entrance to the beam tunnel where $B_z = B_{z_0}$. The wall geometry and material clearly have a large effect on the density profile of the traversing beam.

III. Equilibrium - Limiting Current

A method is derived by which the equilibrium velocity and density profiles as well as the limiting current for a beam traversing a smooth beam tunnel may be computed. The degree to which the limiting current is reduced by replacing the smooth tunnel with an absorbing one, due to the effects described in Sec. II, is determined. As the magnetic field is seldom constant in a gyrotron beam tunnel, located just before the interaction cavity, the effects of magnetic field compression are included in the analysis. The

relevant non-relativistic fluid equations for the beam (relativistic equations shown later in this section) are:

$$m n \left[\frac{\partial \underline{v}}{\partial t} + (\underline{v} \cdot \nabla) \, \underline{v} \right] = q \, n \, (\underline{E} + \underline{v} \times \underline{B}) \ ,$$

(1a)

$$\nabla \cdot \underline{B} = 0 \ ,$$

(1b)

$$\nabla \cdot \underline{E} = -\frac{\rho}{\varepsilon_0} \ ,$$

(1c)

$$\frac{\partial n}{\partial t} + \nabla \cdot (n \, \underline{v}) = 0 \ .$$

(1d)

In the above equations a monoenergetic beam is assumed. Further, azimuthal symmetry (i.e. $\partial / \partial \Theta = 0$), and knowledge of $B_z(z)$ is assumed. For an equilibrium solution $\partial / \partial t = 0$ is required. Taking the scalar product of Eq. (1a) with $\widehat{\Theta}$, expanding Eq. (1b) to get $B_r = (-r/2) \nabla_z B_z$, and integrating with respect to z, we can derive,

$$\beta_\perp = \beta_{\perp_0} \left(\frac{B(z)}{B_0} \right)^{\frac{1}{2}} \ ,$$

(2)

where $\beta_\perp = v_\perp / c$. Equation (2) is conservation of magnetic moment of the electron fluid. Taking the scalar product of Eq. (1a) with $\underline{v}$, it follows that,

$$\beta_z \nabla_z \beta_z + \beta_\perp \nabla_z \beta_\perp = \frac{q E_z}{mc^2} \ .$$

(3)

The expression for E_z is found as $E_z = - \nabla_z \phi$ where ϕ is the solution of Poisson's equation. The exact analytical soution for ϕ however would be intractable for a beam tunnel of the geometry of Fig. 1 and therefore an approximate expression for ϕ will be used. For an annular beam of radius r_b and thickness Δr, with a wall at constant radius,

r_w, the analytical solution of Poisson's equation for the potential at the inner surface of the beam, $r = r - \Delta r/2$, is,

$$\phi = \frac{I_b}{4\pi\varepsilon_0 c \beta_z} \; S\left(\frac{r_b}{r_w}, \frac{\Delta r}{r_w}\right) ,$$

(4)

where,

$$S\left(\frac{r_b}{r_w}, \frac{\Delta r}{r_w}\right) = S(a, b) = 1 - \frac{2\left(a + \frac{b}{2}\right)^2}{\left(a + \frac{b}{2}\right)^2 - \left(a - \frac{b}{2}\right)^2} \; ln\left(a + \frac{b}{2}\right) + \frac{2\left(a - \frac{b}{2}\right)^2}{\left(a + \frac{b}{2}\right)^2 - \left(a - \frac{b}{2}\right)^2} \; ln\left(a - \frac{b}{2}\right) ,$$

(5)

with $a = r_b/r_w$, $b = \Delta r/r_w$. Figure 3 shows contours of S as a function of r_b/r_w and $\Delta r/r_w$. The factor S is shown to be essentially independent of beam width, $\Delta r/r_w$, for all values of r_b/r_w. The approximation $\Delta r \sim 0$ can therefore be used without introducing significant error even for beams of large Δr. Expanding the logarithmic terms of Eq. (5) for small Δr and letting $\Delta r \to 0$, it is found that, $S(r_b/r_w, \Delta r/r_w) \sim S(r_b/r_w, 0) = -2ln(r_b/r_w)$, or,

$$S\left(\frac{r_w}{r_b}\right) = 2 \; ln\left(\frac{r_w}{r_b}\right) .$$

(6)

Since r_w is allowed to change abruptly in the absorbing beam tunnel as well as allowing for dielectric wall material, an average radius, r_{wa}, and an oscillating function, $\tilde{f}_0(z)$, are defined and ϕ is written as,

$$\phi(z) = \frac{I_b}{4\pi\varepsilon_0 c \beta_z(z)} \left(1 + \tilde{f}_0(z)\right) \; S\left(\frac{r_{wa}}{r_{bo}}, \frac{B_z(z)}{B_0}\right) .$$

(7)

where

6

$$S\left(\frac{r_{wa}}{r_{bo}}, \frac{B_z(z)}{B_0}\right) = 2\ ln\left[\frac{r_{wa}}{r_{bo}}\left(\frac{B_z(z)}{B_0}\right)^{1/2}\right] = 2\ ln\left(\frac{r_{wa}}{r_{bo}}\right) + ln\left(\frac{B_z(z)}{B_0}\right) \ . \tag{8}$$

$\tilde{f_0}(z)$ produces the ripple on the potential profiles due to the wall geometry and material $(\tilde{f_0} \equiv 0$ for a smooth conducting wall). r_{wa} is generally near to the average radius of the conductors and the dielectric. Here conservation of flux has been used to allow for changing beam radius with $B_z(z)$. Equation (7) is an approximation valid for slowly varying values of β_z, $\tilde{f_0}$, and S. The effect of rapidly varying quantities is discussed at the end of this section. Figure 1 shows r_{wa} and includes the general form of $(1 + \tilde{f_0})$ for a typical absorbing beam tunnel. The precise form of $\tilde{f_0}$ (always oscillatory about zero) is chosen to give, using Eq. (7), exactly the correct potential depression (computed from Poisson's equation) for a beam of constant density and magnetic field. $\tilde{f_0}(z)$ is therefore a measure of the percentage excursion of ϕ at the inner surface of the beam from the case of a smooth wall. In this way, all effects due to wall geometry and material may be included in the function $\tilde{f_0}(z)$.

Eq. (3) now becomes,

$$\beta_z\ \nabla_z\beta_z + \beta_\perp\ \nabla_z\beta_\perp = -\frac{q}{mc^2}\ \nabla_z\left(\frac{I_b}{4\pi\varepsilon_0 c\beta_z}\ (1+\tilde{f_0})\ S\left(\frac{r_{wa}}{r_{bo}}, \frac{B_z}{B_0}\right)\right) \ . \tag{9}$$

We let,

$$\beta_{x_0}^3 = \frac{q\,I_b}{4\pi\varepsilon_0 mc^3} \ . \tag{10}$$

And differentiating Eq. (2), $\beta_\perp\nabla_z\beta_\perp = (\beta_{\perp_0}^2 / 2B_0)\nabla_z B_z$, substituting into Eq. (9) and integrating from z_0 to z, after rearranging,

$$\left(\frac{\beta_z}{\beta_{z_0}}\right)^3 - \left[1 + 2\frac{\beta_{x_0}^3}{\beta_{z_0}^3}\ S(z_0) - \alpha_0^2\left(\frac{B_z(z)}{B_{z_0}} -1\right)\right]\left(\frac{\beta_z}{\beta_{z_0}}\right) + 2\frac{\beta_{x_0}^3}{\beta_{z_0}^3}\ S(z)(1+\tilde{f_0}(z)) = 0 \ , \tag{11}$$

where $\alpha_0 = \beta_{\perp 0}/\beta_{z0}$. With expression (11), given a magnetic field profile and initial beam conditions $\beta_z(z)$ can be computed as the solution of Eq. (11) at each point in z. With the result of Eq. (1d), $n_0(z) = n_0(\beta_{z0}/\beta_z(z))$, the solution will be a spatially-resolved profile of $\beta_z(z)$, $n_0(z)$ along the beam tunnel for any current below the limiting current. An example is shown in Fig. 4 in which Eq. (11) has been used to compute the equilibrium profile for a beam undergoing magnetic compression and with a beam tunnel for which $\tilde{f}_{0max} = 0.2$. The effect of the walls and of the magnetic compression are clearly seen. To determine the limiting current, $B_z(z) = B_{zmax}$ is chosen and B_c is defined as:

$$B_c = maximum\ beam\ compression\ along\ beam\ tunnel = \frac{B_{z\ max}}{B_{z0}}\ ,\qquad(12)$$

and since B_z is slowly varying with respect to $\tilde{f}_0$, one can choose $\tilde{f}_0 = \tilde{f}_{0max} = \tilde{f}_{0m}$ and also $S = S_{max} = S_m$ simultaneously. At the location of maximum beam compression, Eq. (11) becomes,

$$F\left(\frac{\beta_z}{\beta_{z0}}\right) = \left(\frac{\beta_z}{\beta_{z0}}\right)^3 - \left[1 + 2\frac{\beta_{x0}^3}{\beta_{z0}^3}S_0 - \alpha_0^2\ (B_c - 1)\right]\left(\frac{\beta_z}{\beta_{z0}}\right) + 2\frac{\beta_{x0}^3}{\beta_{z0}^3}S_m\ (1 + \tilde{f}_{0m}) = 0\ ,$$
$$(13)$$

where $S_0 = S(z_0)$. The condition for which no equilibrium exists, i.e., for which the limiting current has been reached is,

$$F\left[\left(\frac{\beta_z}{\beta_{z0}}\right)_i\right] = 0\ ,\qquad(14a)$$

where $(\beta_z/\beta_{z0})_i$ is the solution of

$$\frac{\partial F}{\partial \ (\beta_z / \beta_{zo})} = 0 \ . \tag{14b}$$

The solution of Eqs. (13) and (14) yields an equation for β_{xo}, at the limiting current in terms of β_{zo}, α_0, S_0, B_c, $\tilde{f}_{om}$, and S_m:

$$2 S_0 \left(\frac{\beta_{xo}}{\beta_{zo}}\right)^3 - 3 S_m^{2/3} \ (1 + \tilde{f}_{om})^{2/3} \left(\frac{\beta_{xo}}{\beta_{zo}}\right)^2 + \left[1 - \alpha_0^2 \ (B_c - 1) \ \right] = 0 \ , \tag{15}$$

which can subsequently be solved for the limiting current, I_{bm}:

$$I_{bm} = \frac{4 \pi \varepsilon_0 m c^3 \beta_{zo}^3}{q} \left(\frac{\beta_{xo}}{\beta_{zo}}\right)^3 \ . \tag{16}$$

If $S_0 = 0$ is chosen, the solution for I_{bm} can be written in closed form. This corresponds to a beam launched at $z = z_0^-$ where the wall is at $r_w = r_b$. The '-' indicates a position several tunnel diameters to the negative z side of z_0. The potential depression is therefore zero and the launch conditions can be specified exactly. Otherwise an iterative solution of Eq. (15) is required to find the launch potential depression. With this assumption, the expression for the limiting current from Eqs. (15)-(16) becomes:

$$I_{bm} = \frac{4 \pi \varepsilon_0 m c^3}{3^{3/2} q} \frac{\beta_{zo}^3}{1 + \tilde{f}_{om}} \frac{\left[1 - \alpha_0^2 (B_c - 1)\right]^{3/2}}{2 \ln(r_{wd} / r_b) + \ln B_c} \ . \tag{17}$$

Expression (17) does not include effects of dispersion on the limiting current. This has been addressed elsewhere (Antonsen *et al.* 1986, Tsimring 1990).

The relativistic analog of Eq. (11) can be derived to compute the relativistic velocity and density profiles using conservation of energy and flux:

$$\gamma(z) = \gamma_0 - \frac{q}{mc^2} (\phi(z) - \phi(0)) \ , \tag{18a}$$

9

$$p_\perp^2 = p_0^2 \left(\frac{B}{B_0}\right) ,$$

(18b)

where $\gamma = \left(1 - \beta_z^2 - \beta_\perp^2\right)^{-1/2}$ and $p_\perp = \gamma m v_\perp$. Equation (18a) can be rewritten as :

$$\frac{K_1(z)}{\sqrt{1 - \beta_z^2}} = K_0 - \frac{K_2(z)}{\beta_z} ,$$

(19a)

where,

$$K_0 = \gamma_0 + \frac{\beta_{x_0}^3 \, S_0 \, (1 + \tilde{f}_0(0))}{\beta_{z_0}} ,$$

(19b)

$$K_1(z) = \left[1 + \beta_{\perp_0}^2 \left(\frac{B_z(z)}{B_0}\right) \gamma_0^2\right]^{1/2} ,$$

$$K_2(z) = \beta_{x_0}^3 \, S(z) \, (1 + \tilde{f}_0(z)) .$$

Equation (19a) then becomes:

$$F(\beta_z) = (K_0^2)\beta_z^4 - (2K_2K_0)\beta_z^3 + (K_2^2 + K_1^2 - K_0^2)\beta_z^2 + (2K_2K_0)\beta_z - (K_2^2) = 0 .$$

(20)

Again, given all initial conditions, Eq. (20) can be solved for each point in z to yield the relativistic velocity (and subsequently density) profile in the beam tunnel. As with the derivation of Eq. (17), the condition for which no solution exists, i.e. for which the limiting current has been reached, is determined by:

$$F(\beta_{z_i}) = 0 ,$$

(21a)

where β_{z_i} is the solution of:

$$\frac{\partial F}{\partial \beta_z} = 0 .$$

(21b)

10

This is performed numerically and the solution as a function of launch energy is plotted in Fig. 5 for a gyrotron beam of $r_b/r_{wa} = 0.5$, $\alpha_0 = 1.0$, $B_c = 1.2$, $\tilde{f}_{0m} = 0.2$. This is compared to the non-relativistic solution, Eq. (17), which is seen to be in good agreement at low energies but becomes increasingly far from the relativistic result as launch energy increases. Depending on the beam energy, one can choose the more simple Eqs. (11) and (17) to compute the velocity and density profiles and limiting current for the non-relativistic case, or Eq. (20) for beam energies above 50-$100keV$ depending on the desired accuracy.

The advantage of using this approach to determine the limiting current over merely iterating on the solution of $\beta_z^2 = 2q\phi/mc^2$ is that Eqs. (15), (16), and (20) allow for magnetic field beam compression and for an absorbing beam tunnel. To illustrate, the case of a smooth beam tunnel ($\tilde{f}_0 \equiv 0$, $r_{wa} = r_w$) is first considered. Launch α (α for which the potential depression is zero) vs. limiting current is plotted in Fig. 6(a) for $r_b/r_{wa} = 0.1$. The values plotted are the relativistic self-consistent solutions of Eqs. (20) - (21). Curve (A) is the standard $B_z(z) = constant$ case and is consistent with other published values (Drobot et al. 1981, Ganguly et al. 1984). Curves (B), (C), (D), and (E) are plotted for magnetic compression values of $B_c = 1.2$, 1.4, 1.6, and 1.8, respectively. Note that curves (B) - (E) are not merely curve (A) adjusted in α for a given magnetic compression. One sees that the limiting current is strongly affected by even a slightly increasing tunnel magnetic field. For example, in Fig. 6(a) at $\alpha = 1.5$, an increase in B_z of 20% results in a decrease of the limiting current by over 60%.

The solution of the equations given a launch α will yield a beam potential depression at $z = z_0$ at the limiting current which will retard the beam as, $\beta_{z_0}^2 = \beta_{z_0}^{2^-} - (2q\phi_0/mc^2)$, $\alpha_0 = \sqrt{E_{\perp_0}/E_{z_0}}$, $E_0 = E_{\perp}^- + E_{z_0} = E_{\perp}^- + E_z^- - q\phi_0$. The values printed along the curves (A) - (E) of Fig. 6(a) show the percentage of original beam energy remaining at the current limit, E_0/E^-, the remainder being lost due to the potential depression. For example, a beam launched at $r_b/r_{wa} = 0.10$ with $\alpha = 1.0$ and with a tunnel beam compression of $B_c = 1.2$, has lost over ~15% of its total energy at

the current limit at $z = z_0$. It should be noted that at the limiting current, the value of β_z is not zero. It always retains some positive value, below which no equilibrium solution is possible. Figs. 6(b-e) show the results for values of $r_b/r_{wa} = 0.3, 0.5, 0.7, 0.9$, respectively. The current limits increase for otherwise equivalent beams, since the potential depression decreases as the beam approaches the tunnel wall (Eq. (7) and Fig. 3), illustrating the advantage of using large radius beams.

The case where $\tilde{f}_0 \neq 0$ is now considered, i.e. the case of an absorbing beam tunnel. $\tilde{f}_{0m}$ is the maximum percentage ripple in the beam potential due to the beam tunnel wall. This value is determined by solving Poisson's equation, numerically, for the beam tunnel of interest. Three examples are shown in Figs. 7 which yield values of $\tilde{f}_{0m} = 0.05, 0.15, 0.25$. The geometry of the beam tunnel as well as the dielectric value, ε_r, must be known for this computation. In general, receded dielectrics will yield high values of $\tilde{f}_{0m}$. Low values of ε_r will also yield high $\tilde{f}_{0m}$. Figure 8 shows an example of the change in limiting current for conditions of Fig. 6(d) with $\tilde{f}_{0m} = 0.0$ and $\tilde{f}_{0m} = 0.2$ after Eqs. (20)-(21). The same relativistic as non-relativistic dependence of I_{bm} on $\tilde{f}_{0m}$ is found. Therefore, the limiting current for the relativistic case is seen to vary as $1/(1+\tilde{f}_{0m})$ and the decrease in limiting current between an absorbing and conducting beam tunnel of the same r_{wa} can be written as:

$$- \frac{\Delta I_{bm}}{I_{bm}} = \frac{\tilde{f}_{0m}}{1 + \tilde{f}_{0m}} . \tag{22}$$

Therefore, to include the effect of an absorbing tunnel in the determination of the limiting current, the appropriate plot of Figs. 6 is used to determine I_{bm} for a smooth beam tunnel and this value is decreased by the percentage calculated by Eq. (22). It is seen that this effect can be significant as typical absorbing beam tunnels have $0.05 < \tilde{f}_{0m} < 0.25$ which results in a limiting current decrease of 5% to 20%.

The limiting current of the interaction cavity of a quasi-optical gyrotron may be different from that of the beam tunnel. A reasonable approximation may be made to

determine the limiting current of such a cavity by using Figs. 6 for an $r_{wa} = min(L/2,$ $r_{wc})$ (Alberti 1991) where L is the axial extent of the cavity and r_{wc} is the distance between the axis and the mirrors. For this case, one will most likely use curve (A) of Figs. 6 since the magnetic field profile is usually flat in the interaction cavity. Genoni (1987) presents an exact numeric method of determining cavity limiting current at $B_c = 1$.

As mentioned earlier, in the expressions (7) and (8) for the potential depression ϕ, a slowly varying $\beta_z(z)$, $\tilde{f}_0(z)$, and $S(z)$ has been assumed. If these parameters vary rapidly in z, the variations in the potential will be somewhat less that those estimated by Eqs. (7) and (8). This therefore would result in an estimate of the limiting current somewhat lower than the actual value. Variations in the potential depression as the beam moves axially arise due to magnetic field compression (seen as a change in β_z and S), and wall conditions (seen as a change in β_z (through ϕ) and in $\tilde{f}_0$). Magnetic field compression for all realistic cases is slow enough so as not to affect the estimate of Eq. (7). If the oscillations in $\tilde{f}_0$ are rapid then near the limiting current, depending on the value of λ_0/r_{wa}, Eq. (7) can overestimate somewhat the magnitude of the potential oscillations. Figure 9 shows an expanded view of the actual (dot/dash line) and modeled (solid line) potential profiles for cases of $\lambda_0/r_{wa} = 10, 4, 2, 1$ with density profiles of those near the limiting current for the example geometry given in the figure. (Solution of Eq. (20) for a wide variety of geometries shows that axial oscillations in n_0 at the limiting current are generally of the same magnitude as that of $\tilde{f}_0$.) For large values of λ_0/r_{wa}, the modeled and actual potential profiles will be equal as Eq. (7) is a good approximation to the solution of $\nabla^2 \phi = -\rho/\varepsilon_0$. As λ_0/r_{wa} decreases, the $\partial^2/\partial z^2$ term of the ∇^2 operator becomes larger and Eq. (7) somewhat overestimates the value of the potential oscillations, as seen in Figs. 9(b-c). This though only occurs near the limiting current where the density is high and where $\lambda_0/r_{wa} \sim 2$-5. For currents lower than the limiting current, the actual and modeled profiles of Figs. 9(a-d) are identical. As λ_0/r_{wa} decreases to less than 1, oscillations in $\tilde{f}_0$ and n_0 become small and Eq. (7) is again a good approximation to the actual profile for all currents.

In Fig. 9, it is also seen that as the factor λ_0/r_{wa} decreases, the effect of the wall geometry on the equilibrium profiles also decreases. Therefore, if one requires a given percentage absorber along the beam tunnel, the smallest perturbation in the beam equilibrium will be made with the smallest period size in the conductor/absorber cycles. A small period size should not significantly affect the tunnel absorption characteristics but would greatly reduce the wall's effect on the beam.

IV. Space-Charge Instability

The fluid equations of motion will now be examined to determine the stability characteristics of a beam in the oscillating equilibrium potential profile of an absorbing beam tunnel. The force balance equation (1a) is linearized to get:

$$\frac{\partial \underline{v}_1}{\partial t} + \underline{v}_1 \cdot \nabla \underline{v}_0 + \underline{v}_0 \cdot \nabla \underline{v}_1 = \frac{q}{m}(\underline{E}_1 + \underline{v}_1 \times \underline{B}_0) , \tag{23}$$

where $\underline{v} = \underline{v}_0 + \underline{v}_1$, $\underline{E} = \underline{E}_0 + \underline{E}_1$, and $\underline{B} = \underline{B}_0 + \underline{B}_1$. Here, second order terms have been neglected and the equilibrium solution, $(\underline{v}_0 \cdot \nabla)\underline{v}_0 = (q/m)(\underline{E}_0 + \underline{v}_0 \times \underline{B}_0)$, for the beam has been used in deriving Eq. (23). For this section IV on stability, the subscripted zeros indicate equilibrium quantities and subscripted ones indicate perturbed quantities. Expanding the second and third terms of Eq. (23) assuming azimuthal symmetry and small radial motion (i.e. $\partial/\partial\Theta = 0$, $\underline{v}_r = 0$, $\partial/\partial r = 0$) and allowing only for axial perturbations (i.e. $v_{1\Theta} = 0$), the $\hat{z}$ component of Eq. (23) becomes:

$$\frac{\partial v_{1z}}{\partial t} + v_{1z} \nabla_z v_{0z} + v_{0z} \nabla_z v_{1z} = \frac{q}{m} E_{1z} , \tag{24}$$

In the same fashion, the continuity equation (1d) is linearized:

14

$$\frac{\partial n_1}{\partial t} + n_0 \, \nabla_z v_{1z} + v_{1z} \, \nabla_z n_0 + n_1 \, \nabla_z v_{0z} + v_{0z} \, \nabla_z n_1 = 0 \ . \tag{25}$$

The set of Eqs. (24) and (25) is closed with the expression for E_{1z} which takes one of two forms depending on the magnitude of the oscillation wave number. For slowly spatially varying quantities (small k_z), the electric field will be dominated by the geometry of the tunnel and the linearized form of Eq. (7) is used:

$$E_{1z} = - \, \nabla_z \, \frac{qAS}{4\pi\varepsilon_0} \left(1 + \tilde{f}_0(z)\right) n_1 \ . \tag{26}$$

(for small k_z)

Here I_b has been written as $qn v_z A$ (A is the cross-sectional area of the beam). For rapidly spatially varying quantities (large k_z), the oscillations will be dominated by local electric fields and we therefore use,

$$\nabla_z \, E_{1z} = \frac{qn_1}{\varepsilon_0} \ . \tag{27}$$

(for large k_z)

Assuming an oscillatory form of n_1 and v_{1z} such that $\partial(n_1, v_{1z})/\partial t = -i\omega(n_1, v_{1z})$ and $\nabla_z(n_1, v_{1z}) = ik_z(n_1, v_{1z})$, the dispersion relations for waves of small and large k_z may be derived from Eqs. (24) - (27):

$$\left(\omega - k_z v_{0z} + i v_{0z}'\right)^2 = k_z^2 v_s^2 \left(1 - \frac{i}{k_z}\frac{n_0'}{n_0}\right)\left(1 + \tilde{f}_0 - \frac{i}{k_z}\tilde{f}_0'\right) \ , \tag{28a}$$

(for small k_z)

$$\left(\omega - k_z v_{0z} + i v_{0z}'\right)^2 = \Omega_p^2 \left(1 - \frac{i}{k_z}\frac{n_0'}{n_0}\right) \ , \tag{28b}$$

(for large k_z)

15

where $v_s^2 = (q^2 A S n_0/4\pi\varepsilon_0 m) = \Omega_p^2 \ (AS/4\pi)$ and Ω_p is the local plasma frequency. Here the primed quantities denote derivatives with respect to z. Note that for waves of large k_z, the dispersion relation for $v_{0_z}' = n_0' = 0$ (smooth wall case), reduces to $\omega = k_z v_{0_z} \pm \Omega_p$, the dispersion relation for laminar electron flow.

The stability properties of the waves whose dispersion relation is given by Eqs. (28) can now be examined. For the small k_z case, the oscillation frequency can be solved as:

$$Re(\omega) = k_z v_{0_z} \pm \frac{k_z v_s}{\sqrt{2}} \left(\frac{\tilde{f_0}'}{k_z^2}\frac{n_0'}{n_0} - 1 - \tilde{f_0}\right)^{1/2} \left[\left(1 + \frac{\left(\frac{\tilde{f_0}'}{k_z} + \frac{1 + \tilde{f_0}}{k_z}\frac{n_0'}{n_0}\right)^2}{\left(\frac{\tilde{f_0}'}{k_z^2}\frac{n_0'}{n_0} - 1 - \tilde{f_0}\right)^2}\right)^{1/2} - 1\right]^{1/2} ,$$

(29a)

$$Im(\omega) = \gamma = -v_{0_z}' \pm \frac{k_z v_s}{\sqrt{2}} \left(\frac{\tilde{f_0}'}{k_z^2}\frac{n_0'}{n_0} - 1 - \tilde{f_0}\right)^{1/2} \left[\left(1 + \frac{\left(\frac{\tilde{f_0}'}{k_z} + \frac{1 + \tilde{f_0}}{k_z}\frac{n_0'}{n_0}\right)^2}{\left(\frac{\tilde{f_0}'}{k_z^2}\frac{n_0'}{n_0} - 1 - \tilde{f_0}\right)^2}\right)^{1/2} + 1\right]^{1/2}$$

(29b)

(for small k_z)

In the above, $(\tilde{f_0}'/k_z^2) \, (n_0'/n_0) > (1 + \tilde{f_0})$ is assumed. If $k_0 = $ the equivalent "wavenumber" of the axial oscillations in $\tilde{f_0}$ or equivalently v_{0z} or n_0, and the limit is taken as $(k_0 / k_z) >> 1$, then Eqs. (29) become:

$$Re(\omega) = k_z v_{0_z} \pm \frac{k_z v_s}{2} \left(\frac{\tilde{f_0}'}{k_z} + \frac{1 + \tilde{f_0}}{k_z}\frac{n_0'}{n_0}\right)\left(\frac{\tilde{f_0}'}{k_z^2}\frac{n_0'}{n_0}\right)^{-1/2}$$

(30a)

$$Im(\omega) = \gamma = \upsilon_{0_z} \frac{n_0'}{n_0} \pm \upsilon_s \left(\tilde{f_0}' \frac{n_0'}{n_0} \right)^{1/2} \qquad (30b)$$

where $\upsilon_{0_z}' = -\upsilon_{0_z} (n_0'/n_0)$ has been used. The second term on the right hand side of Eq. (30a) varies with current, beam size, and k_z for a given tunnel but is seen to be typically a fraction of Ω_p for the largest k_z allowed by the model. Eq. (30b) shows that the oscillations are unstable ($Im(\omega) > 0$) for:

$$\upsilon_{0_z} \frac{n_0'}{n_0} > 0 \ . \qquad (31)$$

Note that $\tilde{f_0}' \, n_0'$ is always positive. Therefore, when the velocity is directed along the density gradient, these oscillations are unstable and increase in growth rate as υ_s, or equivalently, density or current increase. One should remember that in an absorbing beam tunnel, condition (31) is satisfied over only part of the beam path. The magnitude of γ will be examined later in this section.

Considering now the stability properties for large k_z oscillations, Eq. (28b) is used to derive:

$$Re(\omega) = k_z \upsilon_{0_z} \pm \frac{\Omega_p}{\sqrt{2}} \left[\sqrt{1 + \left(\frac{n_0'/n_0}{k_z} \right)^2} + 1 \right]^{1/2} , \qquad (32a)$$

$$Im(\omega) = \gamma = \upsilon_{0_z} \frac{n_0'}{n_0} \pm \frac{\Omega_p}{\sqrt{2}} \left[\sqrt{1 + \left(\frac{n_0'/n_0}{k_z} \right)^2} - 1 \right]^{1/2} . \qquad (32b)$$

Taking the limit for $(k_0 / k_z) << 1$, Eqs. (32) become:

$$Re(\omega) = k_z \upsilon_{0_z} \pm \Omega_p , \qquad (33a)$$

$$Im(\omega) = \gamma = \upsilon_{0_z} \frac{n_0'}{n_0} \pm \frac{\Omega_p}{2} \left(\frac{n_0'/n_0}{k_z} \right) . \qquad (33b)$$

Like condition (31), for large k_z, the velocity is required to be directed along the density gradient for the instability to occur and it is seen that increasing density, or equivalently, increasing beam current or launch α will increase the growth rate. The method of Briggs (1964) has been applied to determine the characteristics of the instability described by the dispersion relation (28b). Mapping of the complex roots of Eq. (28b) from the complex ω plane to the complex k plane show that the root described by Eq. (33b) represents a convective amplifying instability. A perturbation occurring at the input to a beam tunnel will propagate its length, amplifying in z. The average growth rate can be calculated as:

$$\overline{\gamma}(z) = \frac{1}{t - t_0} \int_{z_0}^{z} \frac{\gamma(z)}{v_{0z}}\, dz \ ,$$

(34)

where $t = \int dz/v_{0z}$. This calculation will be performed after deriving an approximate expression for the maximum possible growth rate.

A relation between n_0 and $\tilde{f_0}$ from current and energy conservation and Eq. (7) can be derived assuming small axial variations in n_0 and $\tilde{f_0}$:

$$\frac{n_0 - n_0(0)}{n_0(0)} \sim \frac{(v_s/v_{0z})^2}{1 - (v_s/v_{0z})^2}\ (\tilde{f_0} - \tilde{f_0}(0)) \ ,$$

(35a)

and

$$\frac{n_0'}{n_0} \sim \frac{(v_s/v_{0z})^2}{1 - (v_s/v_{0z})^2}\ \tilde{f_0}' \ .$$

(35b)

An example of the growth rate, γ, as a function of k_z is shown in Fig. 10 for a beam with $r_b/r_{wa} = 0.7$, $I_b = 50A$, $E_b = 80keV$, and $\alpha_0 = 1.5$. Once the beam conditions are fixed, the exact form of Fig. 10 becomes dependent only on the choice of $\tilde{f_0}$ and $\tilde{f_0}'$, or equivalently, the choice of the beam tunnel geometry and material. Using the $\tilde{f_0}$ computed from, for example, Fig. 2 ($\tilde{f_{0m}} = 0.15$, $\lambda_0 = 0.01m$), the form of the curve of Fig. 10 is calculated from Eqs. (30b) and (33b). Note that the growth rate decreases to $\gamma = 0$ as $\tilde{f_0}$, $\tilde{f_0}' \rightarrow 0$ and that the distance between the asymptotes for large and small

k_z increases as the beam current increases for an unchanging $\tilde{f}_0$. The assumptions which have been made in deriving the curves for the small and large k_z limit should be recalled. For small k_z, it is required that,

$$\lambda_z \gg r_w \quad \Rightarrow \quad \frac{k_z}{k_0} \ll \frac{\lambda_0}{r_w} \, , \tag{36a}$$

and

$$\left(\frac{n_0'/n_0}{k_z}\right)^2 \gg 1 \quad \Rightarrow \quad \frac{k_z}{k_0} \ll \left(\frac{v_s}{v_{0z}}\right)^2 \tilde{f}_{0m} \, . \tag{36b}$$

For large k_z, it is required that,

$$\lambda_z \ll r_w \quad \Rightarrow \quad \frac{k_z}{k_0} \gg \frac{\lambda_0}{r_w} \, , \tag{37a}$$

and

$$\left(\frac{n_0'/n_0}{k_z}\right)^2 \ll 1 \quad \Rightarrow \quad \frac{k_z}{k_0} \gg \left(\frac{v_s}{v_{0z}}\right)^2 \tilde{f}_{0m} \, . \tag{37b}$$

For the case of Fig. 10, $(v_s/v_{0z})^2 = 0.14$, making the limit condition $k_z/k_0 < 0.025$ for the small k_z limit and $k_z/k_0 > 1$ for the large k_z limit. In Fig. 10, γ/Ω_{ce} has been plotted for an arbitrary magnetic field of $B_0 = 1T$, for easy comparison to growth rates of other instabilities. This instability, however, is independent of the value of Ω_{ce} as the oscillations occur parallel to the applied magnetic field. To estimate the maximum growth rate at currents less than the limiting current, $(v_s/v_{0z})^2 \ll 1$ is assumed and Eq. (35b) becomes $n_0'/n_0 = (v_s/v_{0z})^2 \tilde{f}_0'$ and consequently the maximum growth rate, γ_m, from Eqs. (30b) and (33b) is:

$$\gamma_m = \frac{\upsilon_s^2}{\upsilon_{0z}} \tilde{f}_0' .$$

(38)

It follows that:

$$\frac{\gamma_m}{S \tilde{f}_0' c} = \frac{2qI_b}{4\pi\varepsilon_0 m c \upsilon_z^2} .$$

(39)

The contours of $\gamma_m/S\tilde{f}_0'c$ are shown in Fig. 11 as a function of I_b and α_0. The calculation was completed for values of α_0 and I_b for which $(\upsilon_s/\upsilon_{0z})^2 < 0.2$. If the growth rate from Fig. 11 for a typical gyrotron beam of $I_b = 50A$, $\alpha_0 = 1.5$ is taken, it is seen that $\gamma/(S\tilde{f}_0'c) \sim 0.07$. Using the CRPP values of $\tilde{f}_0' = k_0\tilde{f}_{0m} = (2\pi/0.01m)(0.15) = 94.2m^{-1}$, $S = 2ln(1.0/0.56) = 1.16$, $\gamma_m = 2.3\times10^9s^{-1}$, gives $\gamma_m/\Omega_{ce} = 1.4\times10^{-2}$ for an axial field of $B_0 = 1T$.

The integral of Eq. (34) using expression (33b) can now be performed as an estimate of $\overline{\gamma}$ in an actual beam tunnel for large k_z. Two cases are considered. The first, an actual beam tunnel and the second $\overline{\gamma}$ is estimated for a beam entering a quasi-optical gyrotron cavity. For the beam tunnel, the solution of Eq. (20) is used yielding the axial equilibrium profiles required for Eq. (33b). The parameters of the beam are given in the figure. The result is shown in Fig. 12. An average positive growth rate of $\overline{\gamma}/\Omega_{ce} = 13\times10^{-3}$ is seen for this case. The oscillations on the $\overline{\gamma}$ curve are due to the changing sign of n_0'/n_0 as the beam moves in z. The net $\overline{\gamma}$ is seen to be positive however for any case in which $B_c > 1$. In Fig. 13, the average growth rate is estimated for a beam entering the interaction cavity of a quasi-optical gyrotron where the scale lengths are much longer than those in the beam tunnel. The potential depression for such a beam is also much larger than that in the beam tunnel as the walls of the interaction cavity are further from the beam. This will slow the beam significantly, increase the density gradient and provide for a large overall $\int n_0'/n_0 \, dz$. The average growth rate over the first half of the cavity is seen to be several times that in the beam tunnel. The growth rate is compared to that of the diocotron instability, known to be present in unneutralized

electron beams. The diocotron instability, arising from azimuthal velocity shear, has a growth rate, γ_b, of $\gamma_b = (G_s / 2)(\Omega_p^2 / 2\Omega_{ce})$, where G_s is a unitless geometric constant dependent on the beam geometry and instability harmonic number s. The maximum value of G_s occurs for thin beams with harmonic numbers above $s \sim 6$ and has a value of $G_{max\ s>6} \sim 0.75$. For the beam conditions at $z = z_0$ of Fig. 13, the maximum diocotron growth rate for $B_0 = 1T$ is $\gamma_b / \Omega_{ce} = 7 \times 10^{-3}$. Though this growth rate varies with beam size, current, magnetic field, etc., it is seen that the growth rate for the axial oscillations described here and for the diocotron instability are of the same order of magnitude for parameters of typical gyrotron beams.

V. Conclusions

A model has been presented which may be used to determine the self-consistent axial density and velocity profiles as well as the limiting current of a beam undergoing magnetic compression in a smooth-walled beam tunnel for a wide range of beam and tunnel parameters. Magnetic compression is seen to decrease the limiting current markedly and it is seen that if a beam is near its limiting current the uniformity of the magnetic field becomes important. It has been shown how to calculate the effect on the velocity and density profiles and limiting current of a beam when the smooth conducting beam tunnel is replaced by an absorbing one. Depending on the geometry and dielectric material, the limiting current may be lowered by as much as *20%* in the most extreme cases. A fluid model has been developed describing a convective instability which arises due to the equilibrium density gradient present in a beam traversing an absorbing beam tunnel in an increasing magnetic field. The instability is also present as the beam enters the interaction cavity where the magnetic field is generally constant. It is electrostatic in nature and results in axial oscillations. These oscillations occur when the beam velocity is directed along the density gradient and the average growth rate has been estimated for large and small values of k_z. The growth rate is seen to increase with increasing current and pitch angle. It is seen that for all values of k_z the growth rate decreases to zero in the

absence of a density gradient brought about by the beam tunnel wall or magnetic field. From a practical standpoint, one would like to minimize the effects of the beam tunnel wall on the equilibrium profiles and limiting current as well as on the stability of the beam as discussed here. One sees that using the smallest possible period size in the conductor/absorber cycles for a given absorber fraction will achieve this result. A small period size, relative to the tunnel radius, will result in a relatively small change in the equilibrium profiles from that of a smooth-walled tunnel. Indeed, modeling shows that if the period size is kept below $\lambda_0 = 0.5r_{wa}$ for any beam with $r_b < 0.7r_{wa}$, the oscillations in the profiles due to the absorbing tunnel wall is less than 5% of the value for a smooth-walled beam tunnel. Choosing a small period size also minimizes the possibility of unwanted cyclotron maser instability oscillations occurring between the tunnel conducting rings.

References

Alberti, S., 1991, Etude expérimentale de l'interaction faisceau d'électrons relativistes - onde électromagnetic dans un gyrotron quasi-optique, *Lausanne report LRP 441/91*.

Antonsen, T., and Levush, B., 1986, *International Journal of Electronics*, **61**, 871-880.

Briggs, R. J., 1964, *Electron-Sream Interaction with Plasmas* (Cambridge: MIT Press).

Drobot, A. T., and Kim, K., 1981, *International Journal of Electronics*, **51**, 351-367.

Ganguly, A. K., and Chu, K. R., 1984, *International Journal of Infrared and Millimeter Waves*, **5**, 103-122.

Genoni, T. C., 1987, *Journal of Applied Physics*, **5**, 3426-3427.

Latham, P. E., 1990, private communication.

Lawson, W., Calame, J., Hogan, B., Main, W., Latham, P. E., Striffler, C. D., Granatstein, V. L., 1990, High Power Microwave Generation from a Two-Cavity Gyroklystron Experiment, In Proc. Fifteenth Int. Conf. on Infrared and Millimeter Waves, Orlando 1990, SPIE Vol. 1514, 669-671.

Tsimring, S. E., 1990, *Radioteckh. Electronics*, **35**, 1284-1288 (in Russian).

<u>Figure captions</u>

Figure 1.   Geometry of beam tunnel and beam showing beam, alternating conducting and absorbing rings, $r_b = beam\ radius$, $\Delta r = beam\ width$, $r_{wa} = effective\ constant\ wall\ radius$. The profile $\tilde{f}_0$ allows for calculation of potential depression given the wall geometry and dielectric material - (a) side view (b) end view.

Figure 2.   (a) Example beam tunnel geometry with potential contours drawn at $-\phi = 0.5,\ 1.5,\ 2.5,\ 3.5,\ 4.5,\ 5.5,\ 6.5keV$. Beam parameters are $E_b = 80keV$, $\alpha_0 = 2.0$, $I_b = 50A$. The contours shown are the solution for a self-consistent density profile. (b) constant (solid) and self-consistent (dotted) density profiles (c) corresponding potential profiles.

Figure 3.   Contours of S for variable r_b/r_{wa} and $\Delta r/r_{wa}$. S is seen to be essentially independent of $\Delta r/r_{wa}$.

Figure 4.   (a) Magnetic field and $\tilde{f}_0$ profiles for a ten-period beam tunnel (b) computed axial density and velocity profiles using Eq. (11) for a beam of $E_b = 80keV$, $\alpha_0 = 1.0$, $I_b = 60A$, $r_b/r_{wa} = 0.5$, $\tilde{f}_{0m} = 0.2$. The current chosen is near the limiting current.

Figure 5.   Limiting current as a funtion of energy for a beam of $\alpha_0 = 1.0$, $r_b/r_{wa} = 0.5$, $\tilde{f}_{0m} = 0.2$, $B_c = 1.2$ for non-relativistic and relativistic solutions.

Figure 6.   (a) Beam alpha vs. limiting current for a beam of $r_b/r_{wa} = 0.1$ and a beam compression of (A) $B_c = 1.0$ (B) $B_c = 1.2$ (C) $B_c = 1.4$ (D) $B_c = 1.6$ (E) $B_c = 1.8$. The values printed along the curves are the percentage of initial total beam energy remaining at the current limit, the remainder being

lost to the potential depression (b), (c), (d), (e) as in Fig. 5(a) for $r_b/r_w = 0.3$, $r_b/r_w = 0.5$, $r_b/r_w = 0.7$, $r_b/r_w = 0.9$, respectively.

Figure 7.   (a) Potential contours in beam tunnel resulting in $\tilde{f}_{0m} = 0.15$ (b) potential profiles for (A) $\tilde{f}_{0m} = 0.05$, ($r_b = 0.32\,cm$, $r_{dielec} = .06\,cm$) (B) $\tilde{f}_{0m} = 0.15$, ($r_b = 0.40\,cm$, $r_{dielec} = .06\,cm$) (C) $\tilde{f}_{0m} = 0.25$, ($r_b = 0.43\,cm$, $r_{dielec} = .08\,cm$). Other parameters as in figure. Beam parameters: $E_b = 80keV$, $\alpha_0 = 1.5$, $I_b = 50A$.

Figure 8.   Limiting current curves for $\tilde{f}_{0m} = 0.0$ (solid) and $\tilde{f}_{0m} = 0.20$ (dotted) after Eqs. (15) and (16) showing the decrease in limiting current for an absorbing beam tunnel.

Figure 9.   Expanded view of the modeled (solid using Eq. (7)) and actual (dot/dash using Poisson's equation) potential profiles in a beam tunnel at the current limit for (a) $\lambda_0/r_{wa} = 10$ (b) $\lambda_0/r_{wa} = 4$ (c) $\lambda_0/r_{wa} = 2$ (d) $\lambda_0/r_{wa} = 1$. Upper (lower) dotted lines show the potential profile for a smooth beam tunnel with $r_{wa} = r_{dielectric}$ ($r_{wa} = r_{conductor}$). For $\lambda_0/r_{wa} \gg 1$, the actual and modeled profiles are identical. At intermediate values, Eq. (7) slightly overestimates the oscillations in the potential profiles and for $\lambda_0/r_{wa} \ll 1$ the oscillations in n_0 and $\tilde{f}_0$ become small and Eq. (7) is again a good approximation. At currents below the limiting current, the solid and dot/dash lines of all figures are identical.

Figure 10.   Instability growth rate, γ/ω_{ce}, as a function of normalized wavenumber, k_z/k_0, shown for large and small k_z asymptotes. For the values plotted here, $\tilde{f}_{0m} = 0.15$, $\lambda_0 = 1\,cm$, $E_b = 80keV$, $\alpha_0 = 1.5$, $I_b = 50A$, $B_0 = 1T$.

Figure 11.   Contours of $10^{-3}\,\gamma_m/(S\,\tilde{f}_0'c)$ vs. I_b and α_0 for $E_b = 80keV$.

Figure 12.   (a) Equilibrium profiles of $n_0/n_0(0^-)$ and β_z using Eq. (20) with a beam of $\tilde{f}_{0m} = 0.15$, $E_b = 80keV$, $\alpha_0 = 1.0$, $I_b = 40A$, $B_c = 1.25$, $r_b/r_{wa} = 0.5$ (the 0^- indicates conditions where the beam depression is defined to be zero) (b) average growth rate, $\bar{\gamma}$, for equilibrium profiles of (a) after Eq (27b). $\bar{\gamma}$ is normalized to Ω_{ce} for $B_0 = 1T$.

grounded
conductor   dielectric

(a)

beam

$\hat{z}$

Δr r_b r_{wa} $(1+\tilde{f}_0(z))r_{wa}$

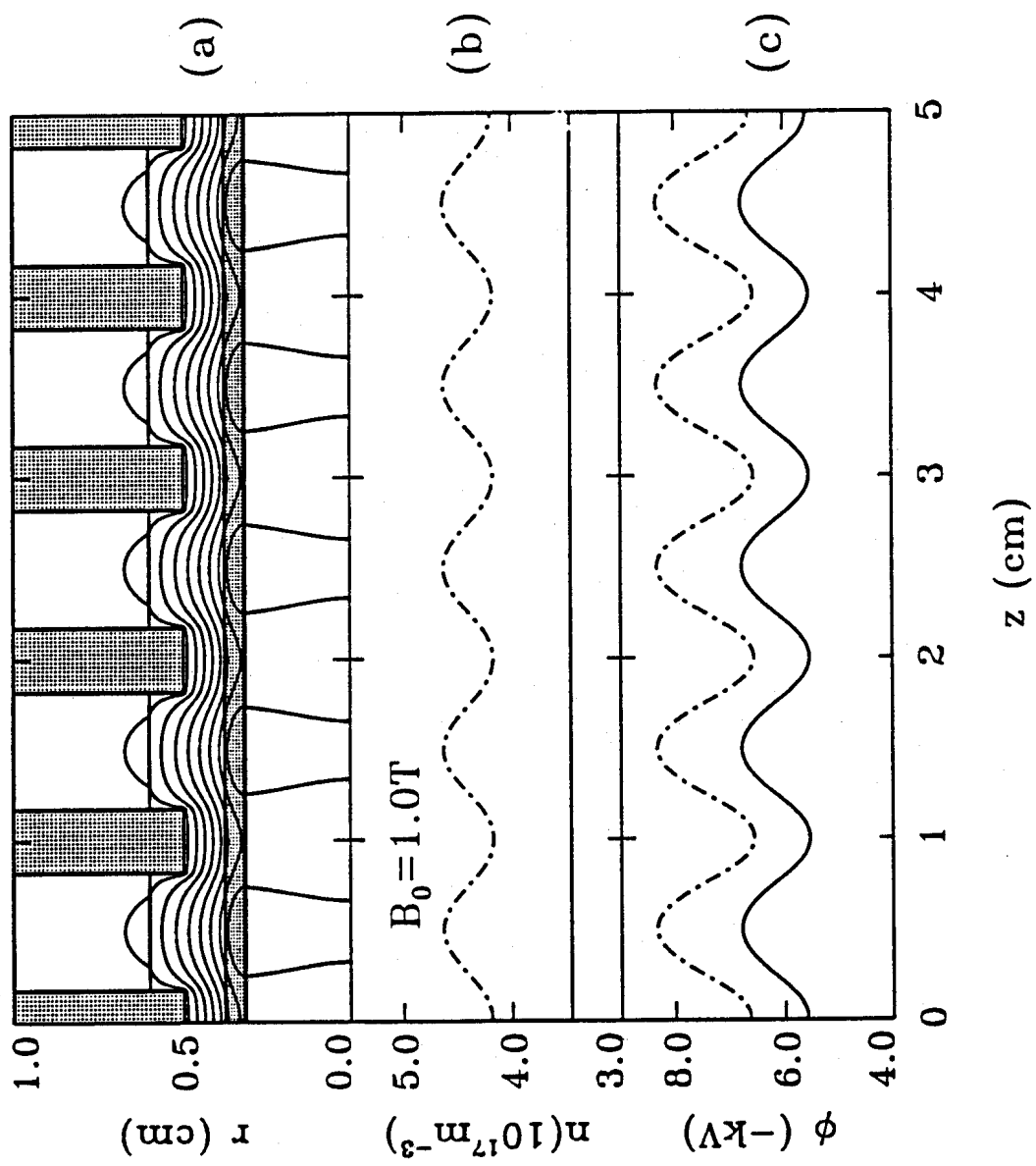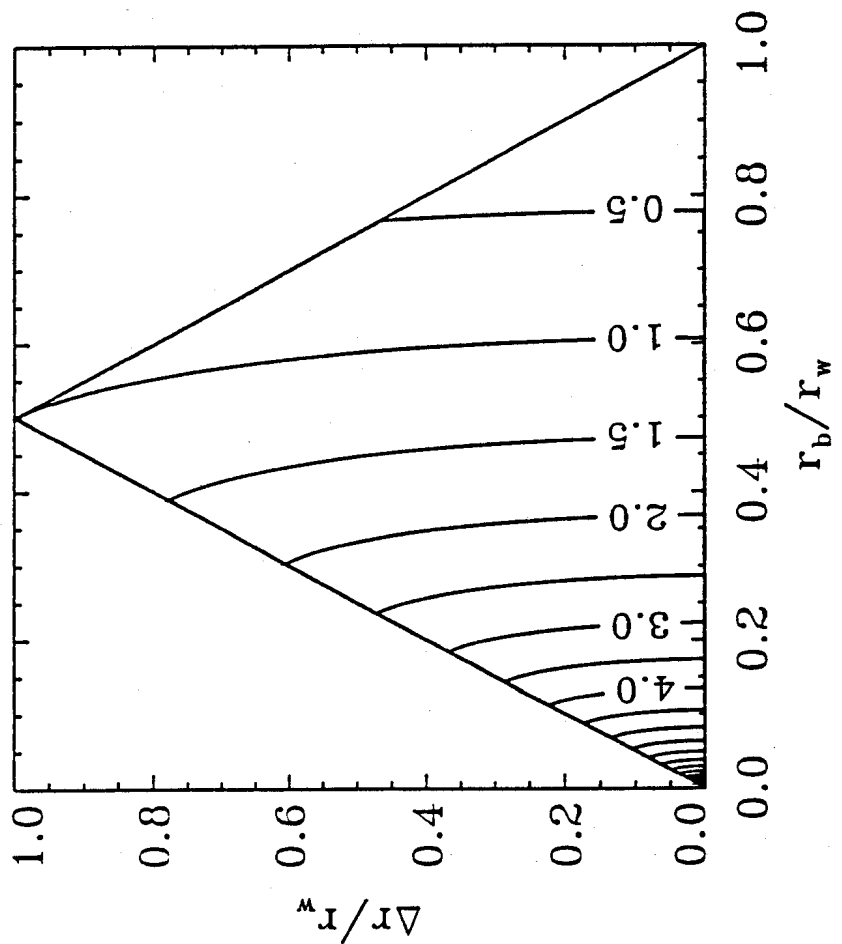$\underline{B}z$

$\stackrel{C}{L}$

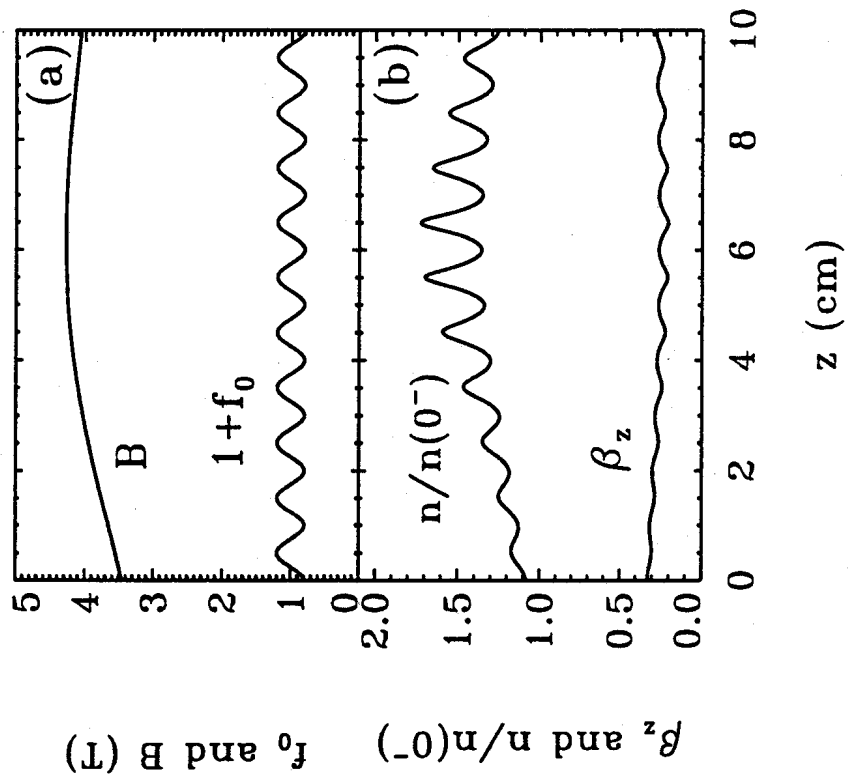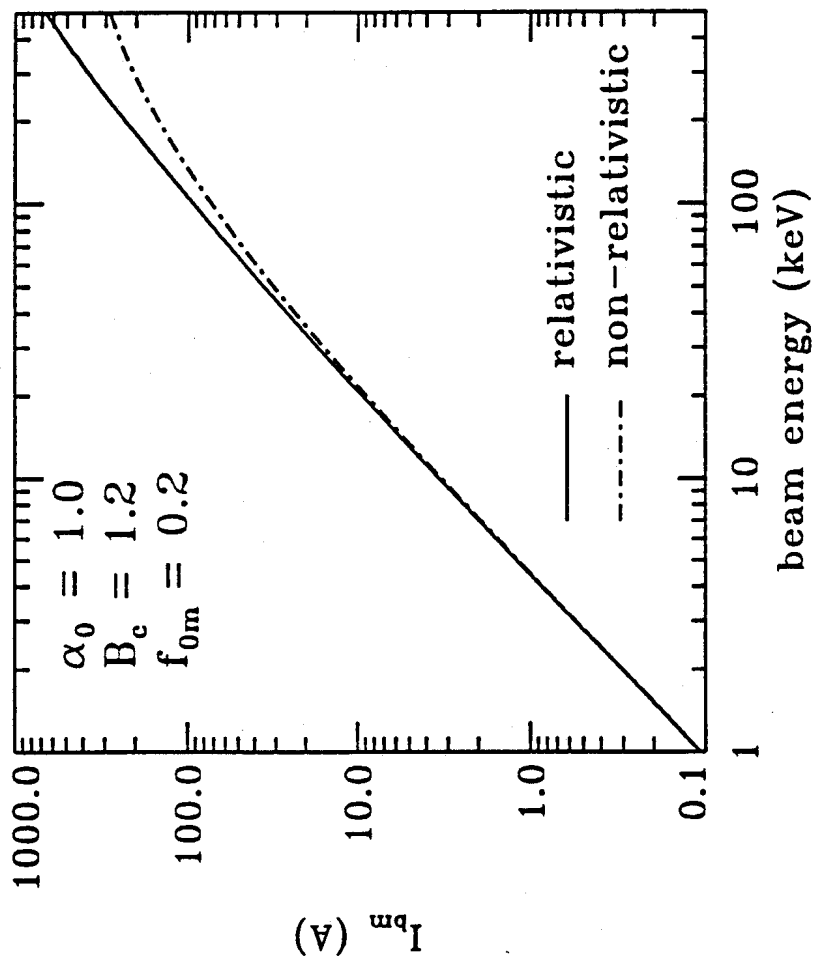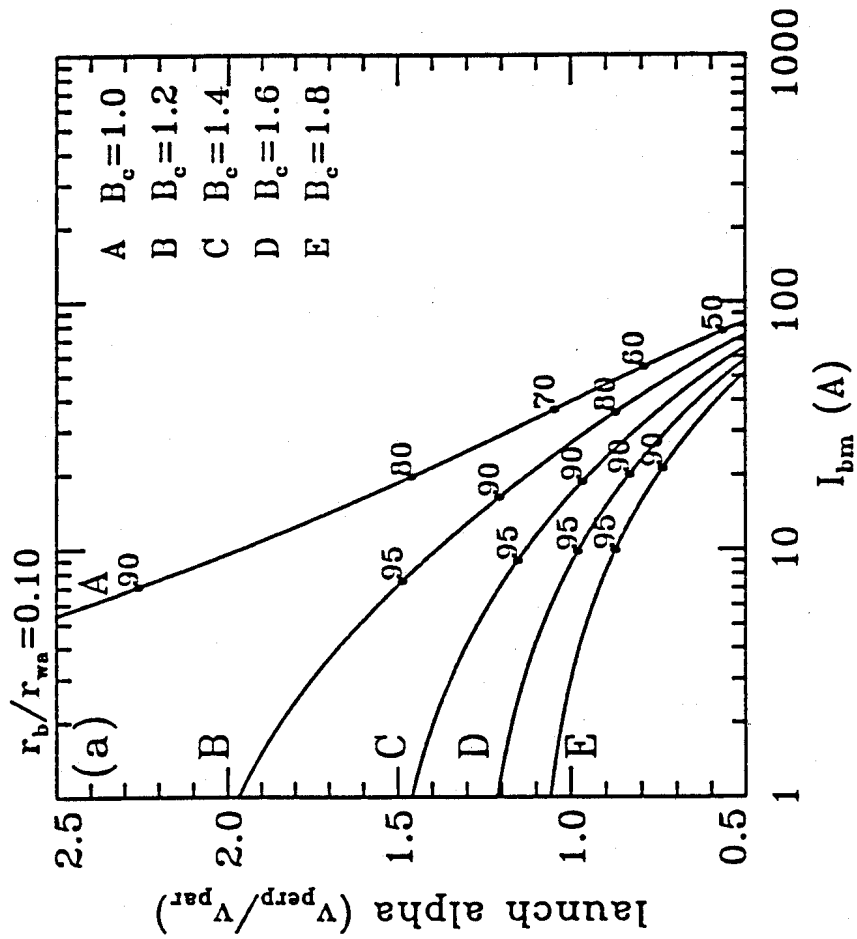(b)

r_b
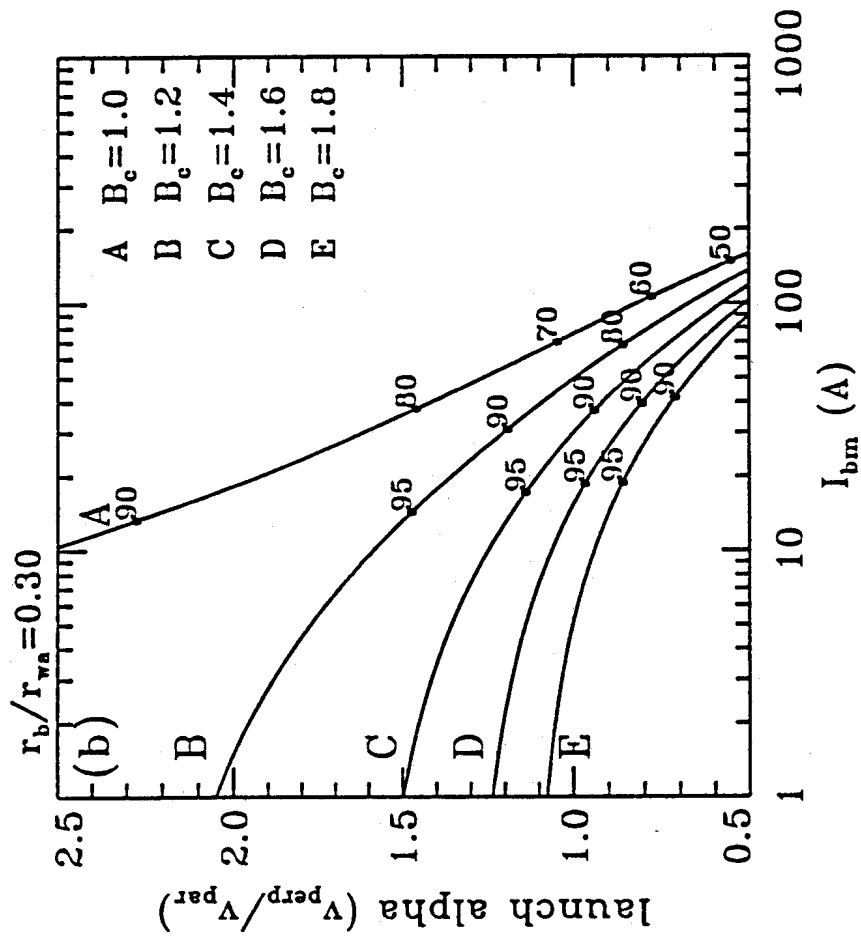
Δr r_{wa}
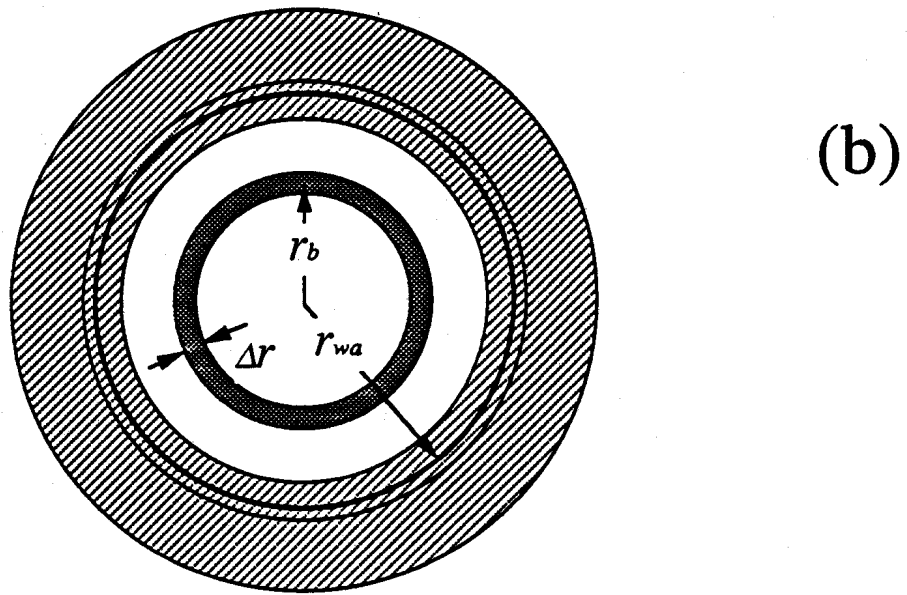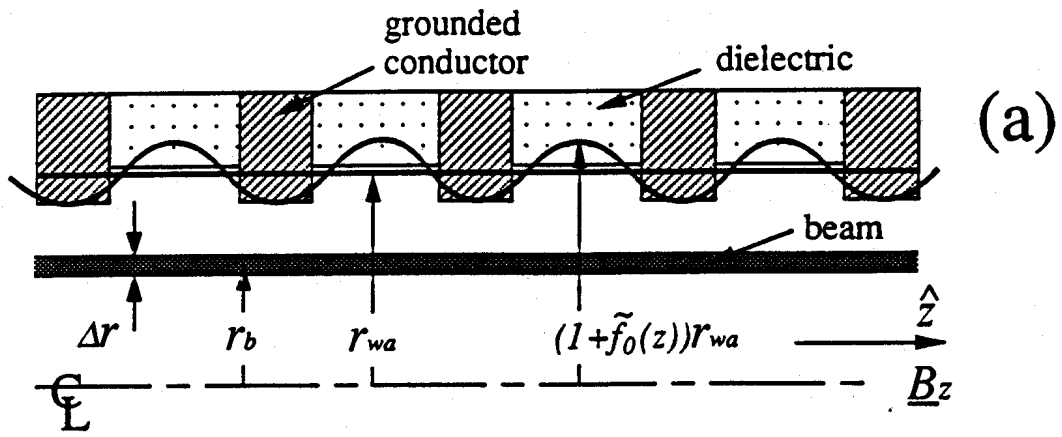
Figure 1.

Figure 2.

Figure 3.

Figure 4.

Figure 5.

Figure 6(a).

Figure 6(b).

Figure 6(c).
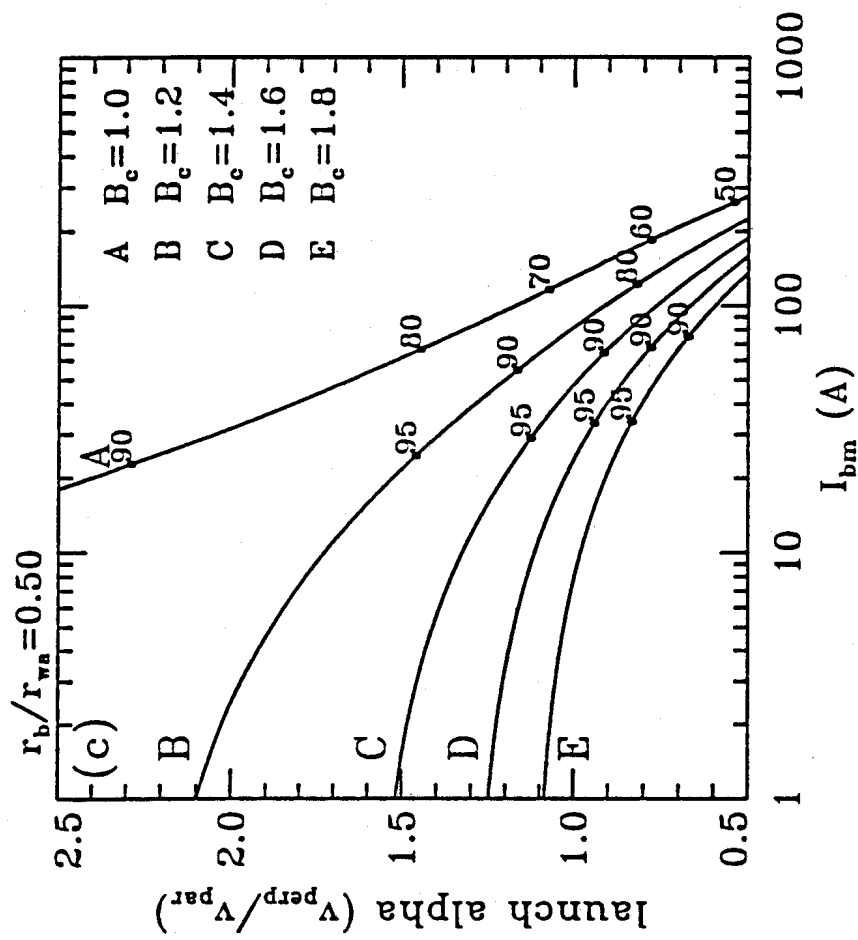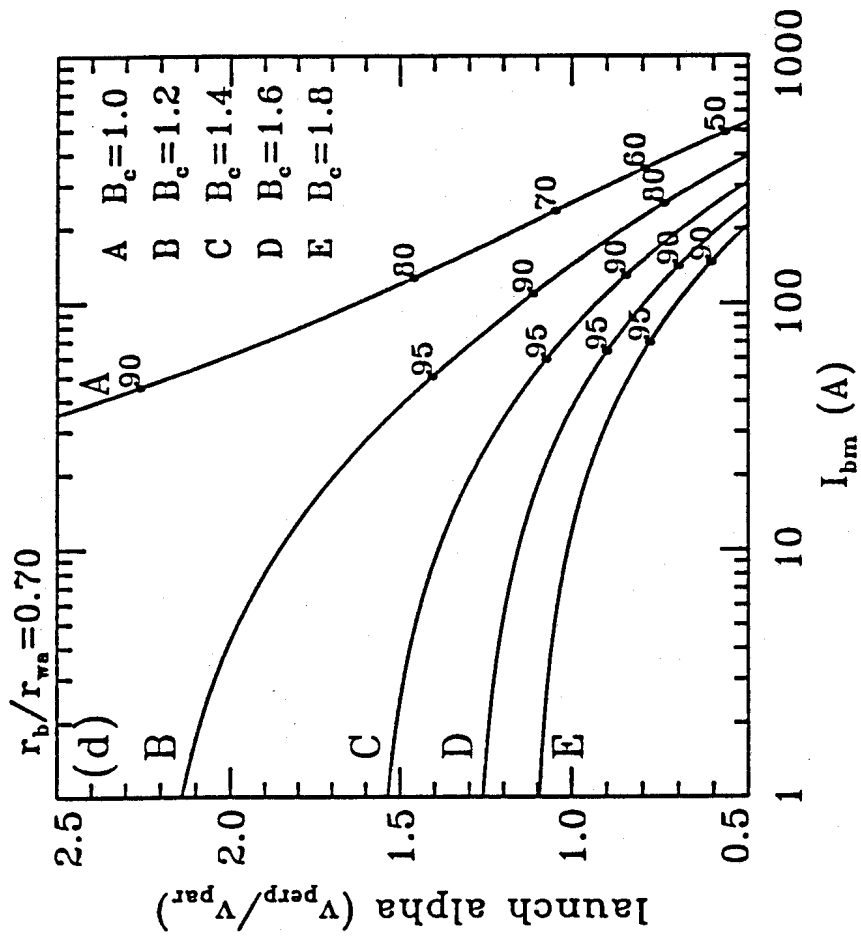
Figure 6(d).

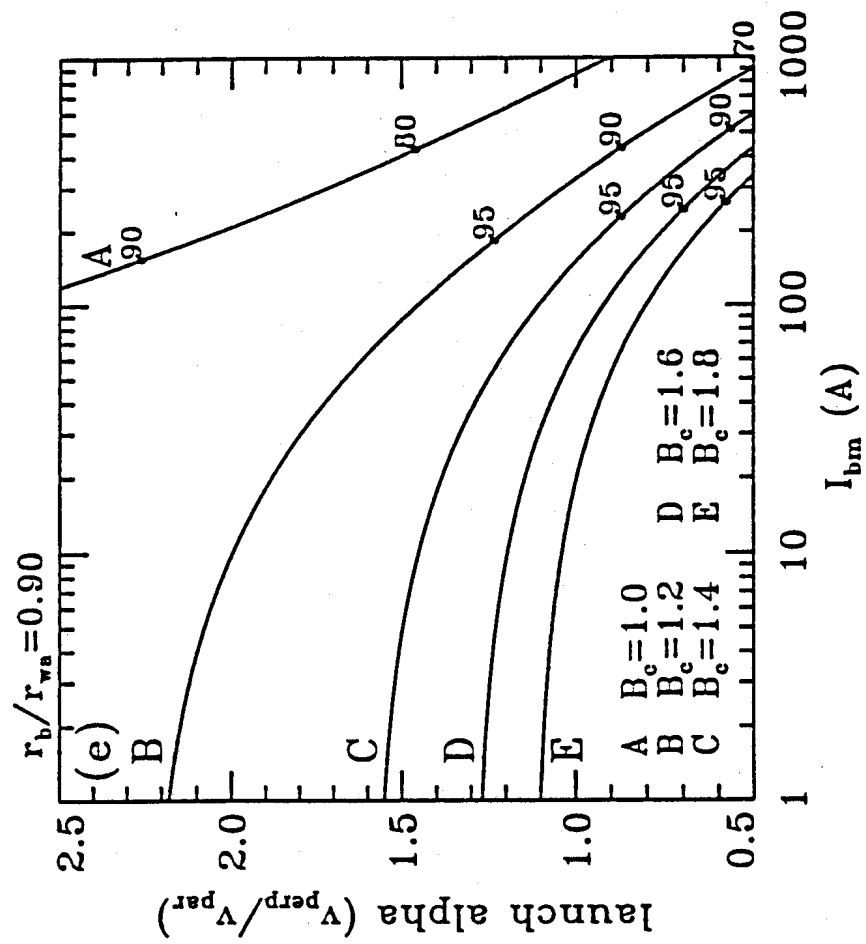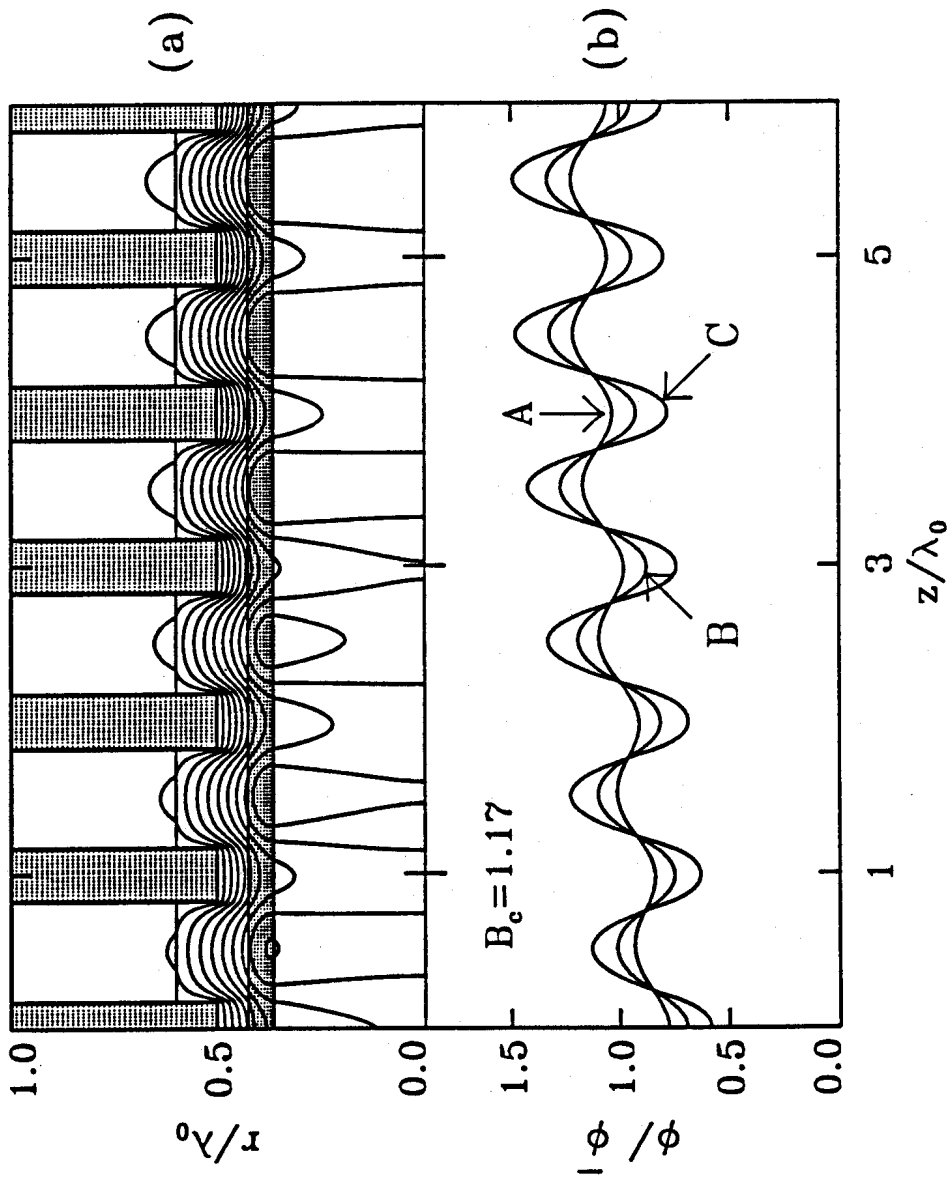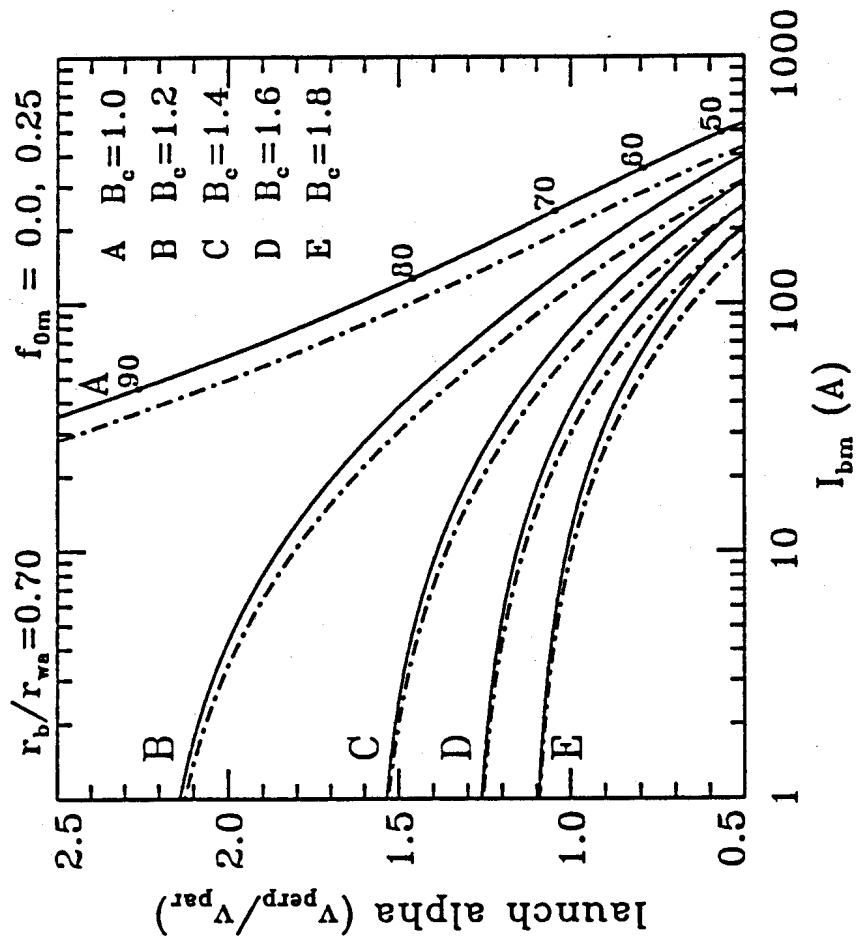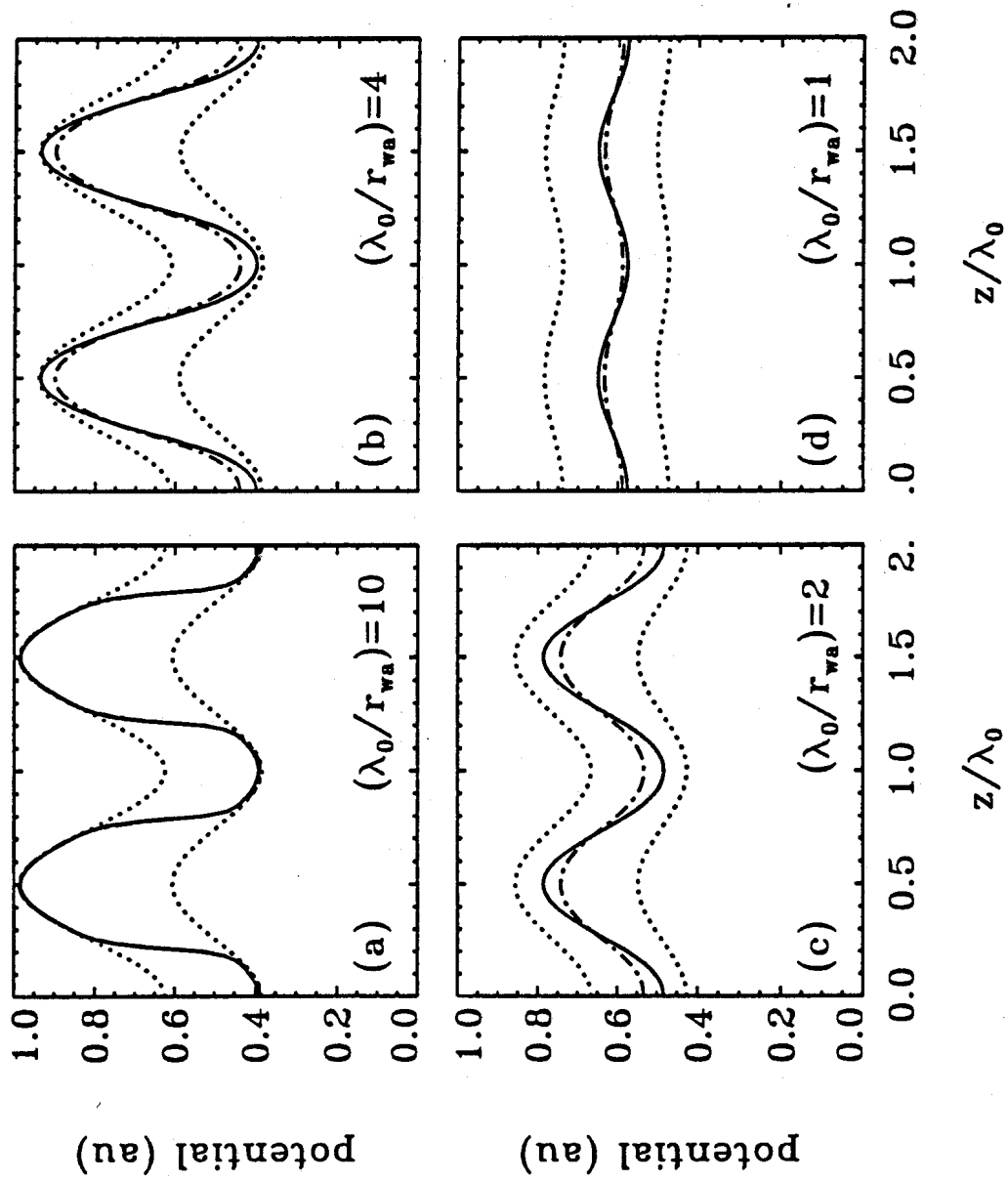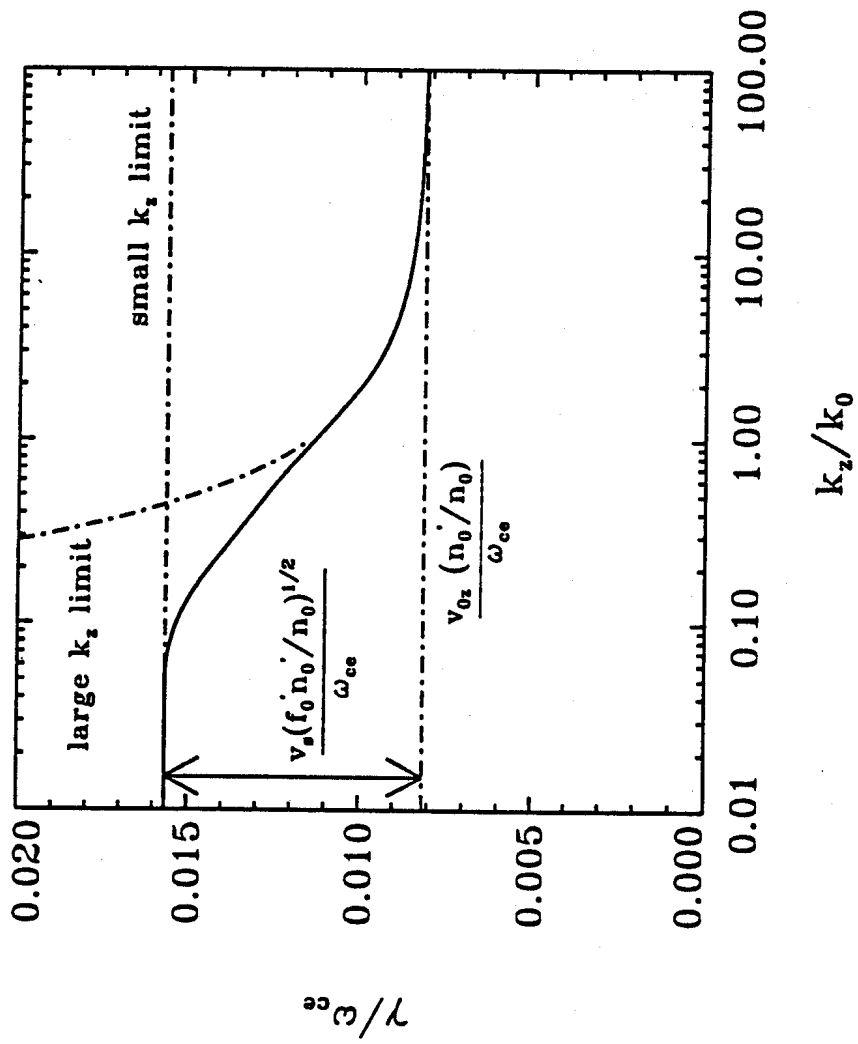Figure 6(e).

(a)

(b)

$B_c = 1.17$

Figure 7.

Figure 8.

Figure 9.

large k_z limit

small k_z limit

$$\frac{v_s (f_0 \dot{n_0}'/n_0)^{1/2}}{\omega_{ce}}$$

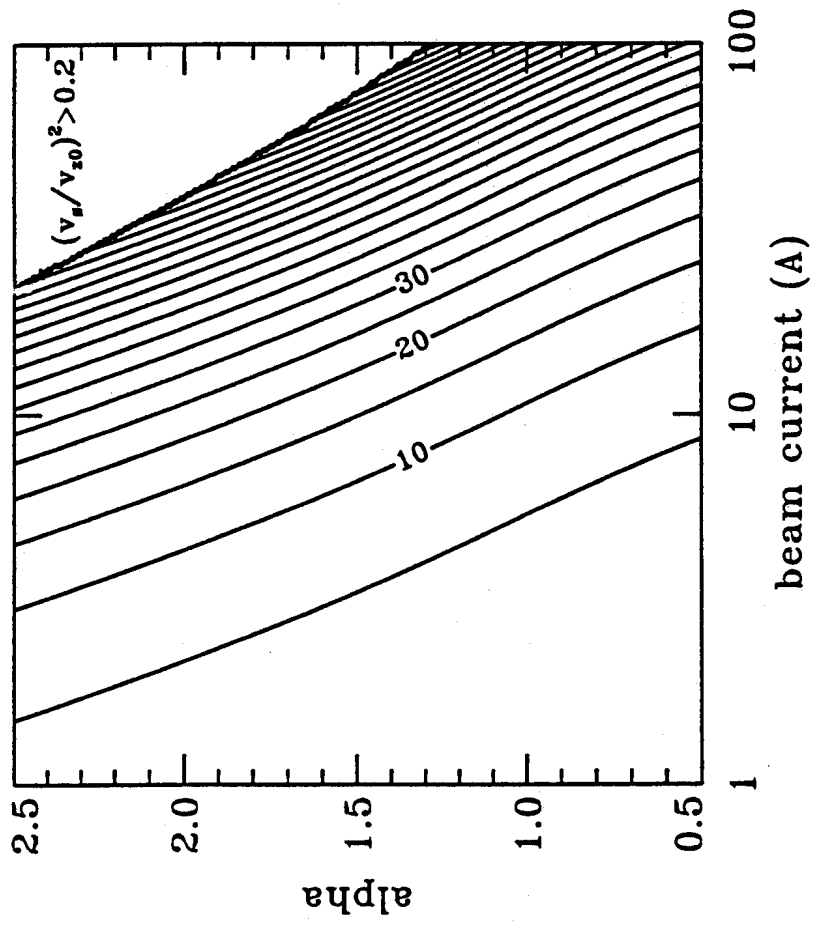$$\frac{v_{0z} (\dot{n_0}'/n_0)}{\omega_{ce}}$$

γ/ω_{ce}
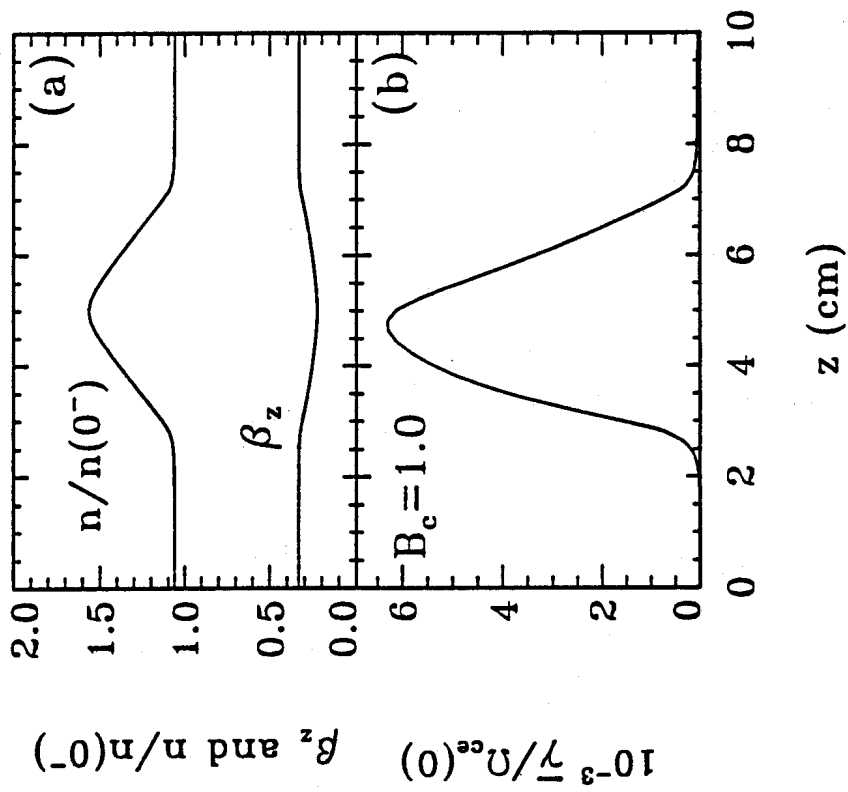
k_z/k_0

Figure 10.

Figure 11.

Figure 12.

Figure 13.